# Investigations of Photolysis and Rebinding Kinetics in Myoglobin Using Proximal Ligand Replacements†

Wenxiang Cao,‡ Xiong Ye,‡ Theodore Sjodin,‡ James F. Christian,‡ Andrey A. Demidov,‡ Svitlana Berezhna,‡ Wei Wang,‡ Doug Barrick,§ J. Timothy Sage,*,‡ and Paul M. Champion*,‡

*Department of Physics and Center for Interdisciplinary Research on Complex Systems, Northeastern University, Boston, Massachusetts 02115, and Department of Biophysics, Johns Hopkins University, 3400 North Charles Street, Baltimore, Maryland 21218*

*Received May 6, 2004; Revised Manuscript Received June 14, 2004*

ABSTRACT: We use laser flash photolysis and time-resolved Raman spectroscopy of CO-bound H93G myoglobin (Mb) mutants to study the influence of the proximal ligand on the CO rebinding kinetics. In H93G mutants, where the proximal linkage with the protein is eliminated and the heme can bind exogenous ligands (e.g., imidazole, 4-bromoimidazole, pyridine, or dibromopyridine), we observe significant effects on the CO rebinding kinetics in the 10 ns to 10 ms time window. Resonance Raman spectra of the various H93G Mb complexes are also presented to aid in the interpretation of the kinetic results. For CO-bound H93G(dibromopyridine), we observe a rapid large-amplitude geminate phase with a fundamental CO rebinding rate that is ∼45 times faster than for wild-type MbCO at 293 K. The absence of an iron proximal ligand vibrational mode in the 10 ns photoproduct Raman spectrum of CO-bound H93G(dibromopyridine) supports the hypothesis that proximal ligation has a significant influence on the kinetics of diatomic ligand binding to the heme.

In myoglobin (Mb),[1] diatomic ligand binding takes place in a highly organized environment formed by surrounding amino acid side chains (*1*, *2*). The proximal side protein residues of Mb, which include the sole covalent attachment between the heme iron and protein through His-93, are thought to have a major influence on the ligand binding kinetics (*3*−*10*). The proximal ligand affects both the electronic structure of the high-spin ferrous iron (*11*, *12*) and the heme geometry [through protein conformational changes (*7*, *8*, *13*)], allowing the proximal side residues to exert control over the energetics of diatomic ligand binding, which takes place on the distal side.

In previous work, we have presented a simple model (*7*) that quantitatively treats the energetics of diatomic ligand binding to heme proteins by partitioning the rebinding barrier into proximal and distal terms, which (for CO binding to Mb) were estimated to be roughly equal in magnitude. Extensive studies, involving the effects of distal pocket mutations on diatomic ligand binding, have been reported by Olson and collaborators (*14*−*26*) and by Sugimoto et al. (*27*). These studies demonstrate that the distal pocket residues in Mb play a major role in controlling the dissociation and migration of diatomic molecules. In contrast, relatively few studies involving proximal ligand perturbations have been carried out (*28*−*33*). As a result, ambiguities remain concerning which residues (proximal or distal) play the dominant role in determining the barriers that control diatomic ligand binding as well as the distribution of these barriers observed below the protein dynamical transition (near 180 K), when the protein conformational fluctuations have been quenched (*16*, *19*, *30*, *33*−*40*).

In this work, we use laser flash photolysis and resonance Raman spectroscopy to investigate the effects of the heme proximal ligand on CO rebinding kinetics. We study adducts of the H93G Mb mutant, where the proximal histidine is replaced by glycine so that imidazole, 4-bromoimidazole, pyridine, or dibromopyridine can bind to the proximal side of the iron in the cavity created by removal of the native His-93 residue (*41*−*47*). The measurements presented here demonstrate that perturbations associated with the proximal heme ligand can dramatically influence the diatomic ligand rebinding kinetics.

## EXPERIMENTAL PROCEDURES

*Sample Preparation.* The sperm whale myoglobin H93G mutant was expressed in *Escherichia coli* and purified as described in detail elsewhere (*41*). The H93G mutant with exogenous proximal ligands was prepared using previously developed procedures (*42*). The exogenous proximal ligands used in this study include imidazole (Im), 4-bromoimidazole (4-BrIm), pyridine (Pyr), and 3,5-dibromopyridine ($Br_2$Pyr). Borate buffer (0.1 M, pH 8.4) with 10 mM Im, 10 mM 4-BrIm, 10 mM Pyr, or saturated $Br_2$Pyr (∼0.2 mM) was used to dilute the H93G stock solution to the desired

† This work was supported by grants from the NSF (0211816 and 0240955) and NIH (DK035090 to P.M.C. and GM-52002 to J.T.S.).

* To whom correspondence should be addressed. P.M.C.: e-mail, p.champion@neu.edu; tel, (617) 373-2918; fax, (617) 373-2943. J.T.S.: e-mail, jtsage@neu.edu; tel, (617) 373-2908; fax, (617) 373-2943.

‡ Northeastern University.

§ Johns Hopkins University.

[1] Abbreviations: Mb, myoglobin; Hb, hemoglobin; Pyr, pyridine; $Br_2$Pyr, dibromopyridine; Im, imidazole; 4-BrIm, 4-bromoimidazole; CO, carbon monoxide; $O_2$, oxygen; NO, nitric oxide; MEM, maximum entropy method.

10.1021/bi049077g CCC: $27.50 
Published on Web 08/06/2004

concentration range. Horse heart myoglobin and wild-type sperm whale myoglobin were purchased from Sigma Chemical Co. and were prepared in 0.1 M phosphate buffer, pH 7. Typical sample concentrations for all measurements were 50−100 $\mu$M.

Nanosecond flash photolysis experiments were performed on samples prepared in cuvettes with 1 mm optical path length. Samples were degassed by repeatedly evacuating the cuvette headspace and flushing with Ar gas. A small amount of degassed dithionite solution was used to reduce the samples. The CO adduct was formed from the reduced samples by flushing with CO for 30 min. Samples used for the Raman experiments were made in gastight vials in a similar way and were transferred into either a stationary 1 mm cuvette or a 10 mm diameter cylindrical spinning cell for Raman experiments.

Sample pH values were measured by a Beckman Instruments Φ40 pH meter. Sample static absorption spectra were obtained using a Hitachi U-3410 spectrophotometer.

*Experimental Setup and Procedures.* The laser flash photolysis experimental setup and procedures have been described in detail previously (*48*). Briefly, a cw beam produced by a universal arc lamp (Oriel Instruments, Model 66021) and a 0.25 m monochromator (Oriel Instruments, Model 77200) probe the kinetic response of the sample at selected wavelengths. The transmitted beam is detected by a high-linearity, low-noise, photomultiplier (Hamamatsu, H6780) and recorded by a transient digitizer (LeCroy 9420). A laser pulse (10 ns, 532 nm), produced by a 10 Hz Nd-doped yttrium−aluminum−garnet (YAG) laser (Continuum, Inc.), is used to photolyze the sample. The pump pulse energy is typically 25 mJ.

The cw resonance Raman setup and data processing have also been reported elsewhere (*49*). The excitation source is either the 413.1 nm line generated by a Kr ion laser (Innova 300; Coherent, Inc.) or the 441.6 nm line from a HeCd laser (Omnichrome 456XM). Light scattered in a right angle geometry (90°) from the sample is collected by lenses and focused into a single grating monochromator (1870B; Spex Industries). An interferometric notch filter (Kaiser Instruments) rejects the intense Rayleigh scattered light. A liquid nitrogen cooled CCD detector (Princeton Instruments), interfaced to a personal computer, records the frequency-resolved intensity of the scattered light. The Raman spectra are calibrated using fenchone as a frequency standard, with a resulting 2 cm$^{-1}$ frequency uncertainty.

The 10 ns transient resonance Raman setup (*50*) is similar to the cw resonance Raman setup. The excitation used to generate time-resolved resonance Raman spectra is derived from 10 ns 532 nm laser pulses produced by a 10 Hz Nd:YAG laser (Continuum, Inc.) and a homemade 50 cm long Raman shifter filled with 185 psi of high-purity hydrogen gas. The resulting anti-Stokes shifted light results in the 10 ns pulses at 435.8 nm. Care is taken to eliminate uneven stress on the 1 cm thick quartz windows at both ends of the Raman shifter cell so that effects due to birefringence are reduced. Two watts of the 532 nm beam was focused with a 30 cm focal length lens into the Raman cell to generate ~10 mW Raman-shifted laser light at 435.8 nm. A dichroic mirror that rejects 532 nm light in a 90° geometry and a blue glass filter were used after the Raman shifter to filter out the 532 nm light and the first red-shifted Stokes line. The scattered Rayleigh light from the sample is attenuated at the monochromator entrance slit by a 442 nm interferometric notch filter (Kaiser Instruments) angle tuned to 435.8 nm. Depending on the details of the scattering geometry, three sharp additional lines sometimes appear in the time-resolved resonance Raman spectra, especially when high-concentration samples are used or if the laser beam scatters off the cuvette surface. These additional lines are positioned at 237, 587, and 1084 cm$^{-1}$ and are removed from the spectra when necessary.

*Measurement of Rate Constants.* A simple three-state kinetic model (*51*) that is widely used to describe the biphasic ligand rebinding process in heme proteins is

$$\mathrm{MbCO} \underset{k_{BA}}{\longleftarrow} \mathrm{Mb{\cdot}CO} \underset{k_{in}}{\overset{k_{out}}{\rightleftharpoons}} \mathrm{Mb} + \mathrm{CO} \qquad (1)$$

Here, MbCO is the CO-bound state, Mb·CO is an intermediate state with the dissociated CO in the distal pocket, and Mb + CO is the state when the photolyzed CO is in the solvent. Within this model (under the condition [Mb] ≪ [CO]), the absorption change as a function of time can be expressed as (*51*)

$$\Delta A(t) = \Delta A_0\{I_g e^{-(k_g t)^\beta} + (1 - I_g)e^{-k_s t}\} = \Delta A_0 N(t) \qquad (2)$$

with $0 \le \beta \le 1$, accounting for short time scale relaxation processes. The protein concentration is denoted by [Mb], and [CO] is the dissolved CO concentration in water: 1.0 mM at 293 K and 1.56 mM at 273 K (*52*). In eq 2, the absorbance change, $\Delta A(t)$, is proportional to the population of the ligand-dissociated heme, $N(t)$, and $\Delta A_0$ is a time-independent normalization factor. The quantity $I_g$ is the geminate rebinding amplitude and $k_g$ and $k_s$ are rate constants for the geminate and bimolecular phases of rebinding, respectively.

The relation between the fundamental rates defined in the three-state model (eq 1) and the observed rates in eq 2 is given by

$$k_{BA} = I_g k_g$$

$$k_{out} = k_g(1 - I_g)$$

$$k_{in} = k_{on}/I_g$$

$$k_{on} = k_s/[\mathrm{CO}] \qquad (3)$$

where $k_{on}$ is the CO concentration-independent bimolecular CO rebinding rate.

## RESULTS

*Kinetics of H93G Myoglobin Mutants.* "Proximally detached" H93G(L) mutants, where the proximal linkage with the protein is ruptured and various heterocyclic nitrogenous ligands (L) bind to the iron in the cavity created by removal of His-93, facilitate the study of proximal influences on diatomic ligand binding (*33*, *41*−*47*). Figure 1 shows the CO recombination kinetics following flash photolysis for wild-type Mb, H93G(Im), H93G(4-BrIm), H93G(Pyr), and H93G($Br_2$Pyr) in buffer. Table 1 lists results from fitting the data in Figure 1, together with the fundamental rates $k_{BA}$, $k_{out}$, and $k_{in}$ calculated using the three-state model in eq 2 and the expressions in eq 3. The bimolecular phase of CO

Table 1: Kinetics of MbCO and Mutant H93G-CO with Various Proximal Ligands

| $T$ (K) | | $I_g$ (%) | $k_g$ ($10^6$ s$^{-1}$) | $\beta$ | $k_{on}$ ($10^6$ s$^{-1}$ M$^{-1}$) | $k_{BA}$ ($10^6$ s$^{-1}$) | $k_{out}$ ($10^6$ s$^{-1}$) | $k_{in}$ ($10^6$ s$^{-1}$ M$^{-1}$) |
|---|---|---|---|---|---|---|---|---|
| 293 | wt Mb | 6.9 | 8.3 | 0.64 | 0.65 | 0.58 | 7.7 | 9.4 |
| | H93G(Im) | 13 | 5.3 | 0.78 | 1.5 | 0.69 | 4.6 | 11 |
| | H93G(4-BrIm) | 18 | 5.9 | 0.64 | 1.8 | 1.1 | 4.8 | 10 |
| | H93G($Br_2$Pyr) | 77 | 34 | 0.67 | 19.6 | 26 | 7.8 | 25 |
| | H93G(Pyr) | 20 | 8.1 | 0.58 | 3.4 | 1.62 | 6.5 | 17 |
| 273 | wt Mb | 11 | 2.5 | 0.53 | 0.27 | 0.28 | 2.2 | 2.5 |
| | H93G(Im) | 21 | 1.7 | 0.67 | 0.52 | 0.36 | 1.3 | 2.5 |
| | H93G(4-BrIm) | 28 | 1.9 | 0.67 | 0.55 | 0.53 | 1.3 | 2.0 |
| | H93G($Br_2$Pyr) | 87 | 22 | 0.60 | 5.3 | 19 | 2.9 | 6.1 |
| | H93G(Pyr) | 26 | 2.4 | 0.57 | 0.87 | 0.62 | 1.8 | 3.3 |

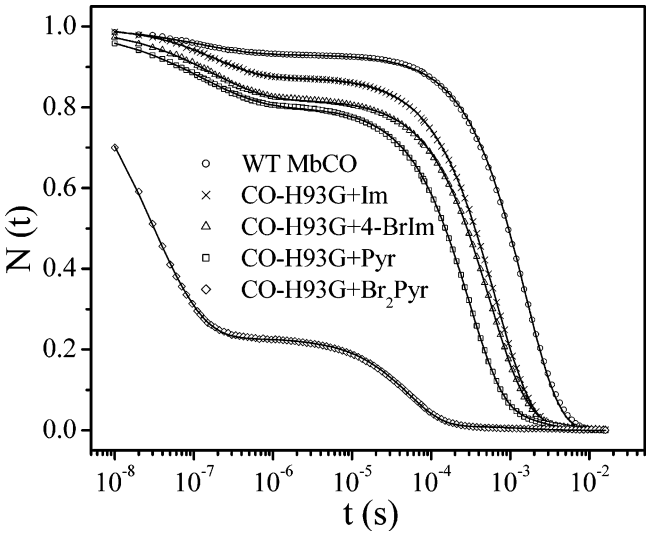


FIGURE 1: CO recombination kinetics for wild-type Mb, H93G-(Im), H93G(4-BrIm), H93G(Pyr), and H93G($Br_2$Pyr), measured at 423, 422, 421, 419, and 415 nm respectively, near the peaks of the reactant Soret bands. The $Br_2$Pyr dramatically changes distal ligand rebinding. The data are normalized according to eq 2.

rebinding to the H93G mutant was sometimes found to deviate slightly from a perfect exponential. To improve these fits, we sometimes supplemented eq 2 by an additional exponential in the long time tail of the bimolecular rebinding or used a maximum entropy (MEM) fitting procedure (*53*). These three different methods for fitting the kinetic rates and the geminate amplitude were all in excellent agreement. For example, when two exponentials were needed to improve the fit to the bimolecular phase [as was the case for H93G-(4-BrIm) and H93G(Im)], the amplitude of the second exponential was always <20%, and the additional rate constant varied by only a factor of ~2 from the primary rate. The geminate amplitude was not affected. The MEM approach yielded a bimolecular rate distribution with a single well-defined peak positioned between the two bimolecular exponential rates. Moreover, the fits obtained with only a single exponential for the bimolecular phase (i.e., eq 2) gave results that were within 10% of the MEM-determined bimolecular rates (which are presented in Table 1). The bimolecular CO rebinding rates, $k_{on}$, at or near 293 K have been reported previously for some of these mutants (*28*, *33*, *54*) and for wild-type myoglobin (*28*, *33*, *54*). Table 2 lists the CO bimolecular rebinding rates for various H93G mutants and wild-type myoglobin along with our measurements for comparison.

Table 1 demonstrates clear quantitative differences in the geminate CO rebinding for different proximal ligands.

Table 2: Comparison of CO Bimolecular Rebinding Rates $k_{on}$ in This Work for Various H93G Mutants with Previous Measurements

| | $k_{on}$ ($10^6$ s$^{-1}$ M$^{-1}$) | |
|---|---|---|
| | this work | other groups |
| wt Mb | 0.65 (293 K) | 0.77 (296 K),[a] 0.51 (293 K),[b] 0.51 (298 K)[c] |
| H93G(Im) | 1.5 (293 K) | 1.7 (296 K),[a] 1.2 (298 K)[c] |
| H93G(4BrIm) | 1.8 (293 K) | 2.0 (296 K)[a] |
| H93G(Pyr) | 3.4 (293 K) | 2.3 (296 K)[a] |

[a] Decatur et al. (*28*). [b] Springer et al. (*54*). [c] Kundu et al. (*33*).

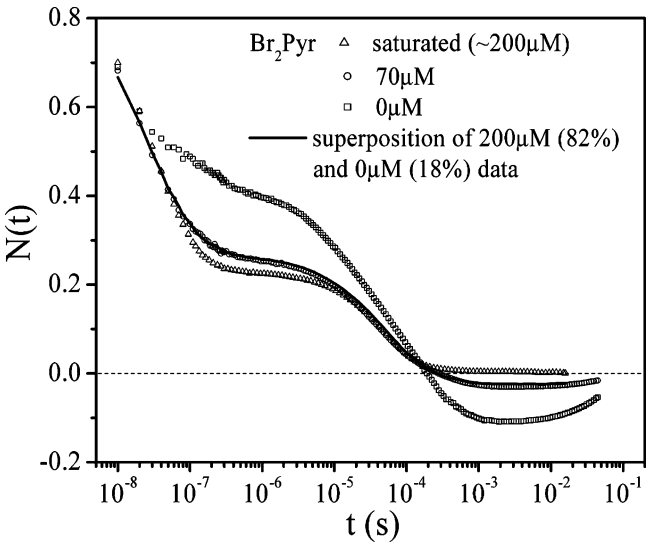


FIGURE 2: CO rebinding kinetics of H93G with various dibromopyridine concentrations measured at 415 nm. The negative absorption change in the bimolecular phase of H93G(0) indicates that at least one additional state participates in the rebinding process. This state must absorb more strongly at 415 nm than the CO-bound H93G(0) starting material ($\lambda_{max}$ = 419 nm). The open circles show the kinetics of an ~40 $\mu$M H93G protein solution containing 70 $\mu$M $Br_2$Pyr. This kinetic response is very well fit using a superposition of the H93G(0) (18%) and the H93G(saturated $Br_2$-Pyr) (82%) kinetics. This demonstrates that a 1:1 complex of H93G and $Br_2$Pyr accounts for the enhanced geminate CO rebinding observed in the 200 $\mu$M $Br_2$Pyr complex.

Modest variations in geminate CO rebinding for differing proximal ligands in H93G were reported in previous measurements, both in water and in 75% glycerol (*29*, *32*, *42*). However, of particular note in the present study is the observation that $k_{BA}$ in CO−H93G($Br_2$Pyr) is 45 times (at 293 K) and 68 times (at 273 K) larger than in wild-type MbCO.

To test the possibility that more than one $Br_2$Pyr ligand is binding to the H93G mutant protein, we varied the $Br_2$Pyr concentration as shown in Figure 2. When the $Br_2$Pyr

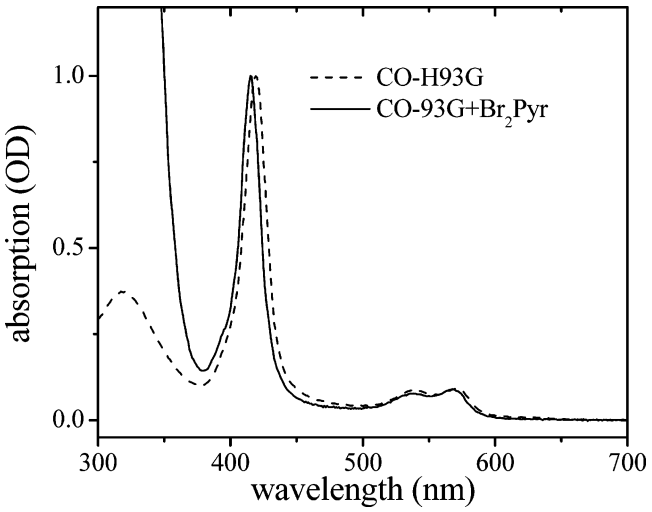


FIGURE 3: Absorption spectra of the CO complex of H93G($Br_2$-Pyr) (solid line) and H93G(0) without heterocyclic nitrogenous ligand (dashed line). The Soret peaks are at 415 and 419 nm for H93G($Br_2$Pyr) and H93G(0), respectively.

concentration is reduced to 70 $\mu$M, so that not all proteins have a $Br_2$Pyr ligand bound, the observed CO rebinding kinetics are well described by a simple linear superposition of the H93G(0) and H93G(saturated $Br_2$Pyr) kinetics. [We use H93G(0) to denote no added exogenous heterocyclic ligand, although it has been suggested (*31*, *55*) that CO binding to H93G(0) leads to proximal ligation by His-97.] The titration kinetics shown in Figure 2 demonstrate that nonspecific binding by $Br_2$Pyr to alternative sites on the mutant protein does not occur. We also note that the H93G-(0) kinetics shown in Figure 2 are multiphasic and display a sign change in the transient signal observed at 415 nm ($-\Delta A_{415}$). Such complex behavior may be indicative of changes in the proximal ligation (*31*, *55*) during CO rebinding to H93G(0) (vide infra).

*Absorption and Raman Measurements of H93G Myoglobin Mutants.* The ligation geometry of H93G($Br_2$Pyr) is unknown, which raises the question of whether $Br_2$Pyr actually enters the heme pocket and binds to the heme iron. If so, does it bind to the proximal or distal side of the heme (or both)? To help to address this question beyond the kinetics shown in Figure 2, we compare the absorption spectra of the CO complexes of H93G with saturated $Br_2$Pyr and of CO−H93G(0) in Figure 3. The blue shift of the Soret band from 419 nm in H93G(0) to 415 nm in the presence of saturated $Br_2$Pyr in Figure 3 indicates that $Br_2$Pyr is in close proximity to the heme and probably bound to the heme iron. Other experimental results (*31*, *55*, *56*) indicate that CO binding to H93G(0) acidifies the iron so that an internal histidine (His-97) binds on the proximal side of the iron. Generally, it has been found (*28*, *42*) that heterocyclic nitrogenous ligands bind to the proximal side of the heme in H93G mutants, and we expect that this applies to $Br_2$Pyr as well.

Figure 4 shows cw resonance Raman measurements in the high- and low-frequency region for deoxy ferrous Mb mutants H93G(Im), H93G(4-BrIm), H93G(Pyr), H93G($Br_2$-Pyr), and H93G(0) together with deoxy horse myoglobin for comparison. The iron−proximal ligand stretching mode (Fe−L) and some core-size markers $\nu_4$, $\nu_3$, and $\nu_2$ are listed in Table 3, along with the force constant between the heme

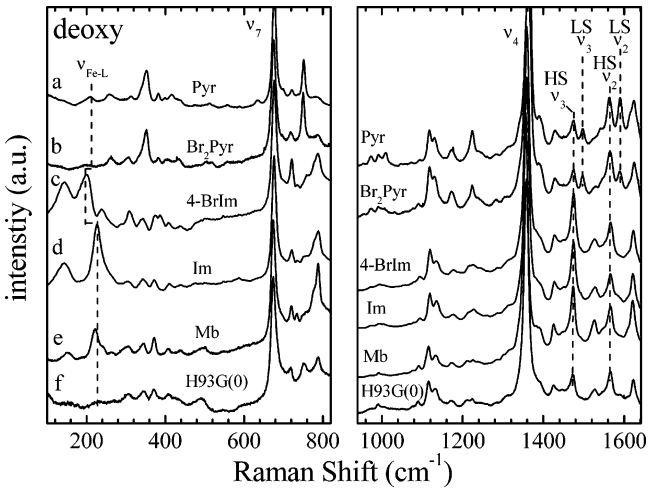


FIGURE 4: Resonance Raman spectra of deoxy (a) H93G(Pyr), (b) H93G($Br_2$Pyr), (c) H93G(4-BrIm), (d) H93G(Im), (e) horse wt Mb, and (f) H93G(0). The wt Mb, H93G(Pyr), H93G($Br_2$Pyr), and H93G(0) samples are excited at 413.1 nm, while H93G(Im) and H93G(4-BrIm) are excited at 441.6 nm. The concentrations of the excess free imidazole, 4-bromoimidazole, and pyridine in buffer solution are 10 mM. The concentration of the excess free dibromopyridine in the buffer solution for H93G($Br_2$Pyr) is saturated, approximately 0.2 mM.

Table 3: Raman Shift of Deoxy Horse Myoglobin and H93G Mutants with Various Ligands in the Proximal Cavity

| | shift ($cm^{-1}$) | | | | | |
|---|---|---|---|---|---|---|
| ligand | $\nu_{Fe-L}$ | $\nu_4$ | $\nu_3$ | $\nu_2$ | MW | $K_{Fe-L}$[a] (N/m) |
| Im | 226 | 1359 | 1474 | 1566 | 68 | 92.6 |
| 4-BrIm | 200 | 1359 | 1474 | 1566 | 147 | 95.8 |
| Pyr | 208 | 1365 | 1474 (HS)<br>1497 (LS) | 1564 (HS)<br>1590 (LS) | 79 | 83.6 |
| $Br_2$Pyr | nd[b] | 1361 | 1475 (HS)<br>1497 (LS) | 1565 (HS)<br>1589 (LS) | 237 | nd |
| 0[c] | nd | 1357 | 1473 | 1566 | nd | nd |
| His(Mb) | 222 | 1356 | 1474 | 1566 | 68[d] | 89.3 |

[a] $K_{Fe-L}$ is the force constant between the heme iron and proximal ligand in a simple two-body oscillator model, $K_{Fe-L} = (2\pi c\bar{\nu}_{Fe-L})^2\mu$. [b] nd = not determined. [c] 0 = no added heterocyclic nitrogenous ligand. [d] Takes account of the mass of the imidazole ring only.

iron and the proximal ligand approximated by using a simple two-body oscillator model

$$K_{Fe-L} = (2\pi c\bar{\nu}_{Fe-L})^2\mu$$

$$\mu = \frac{m_{Fe}m_L}{m_{Fe} + m_L} \quad (4)$$

where $\mu$ is the reduced mass of the heme iron and the proximal ligand. It can be seen that the iron−proximal ligand stretching mode in Figure 4 and Table 3 is sensitive to the proximal ligand, as also observed by Franzen et al. (*57*). Note that the Fe−proximal ligand stretching mode intensity is weak for H93G(Pyr) (trace a) under the solution conditions of Figure 4 and absent for H93G($Br_2$Pyr) (trace b) and H93G-(0) (trace f). The core-size markers for deoxy H93G(Im), H93G(4-BrIm), and H93G(0) have no significant shift relative to horse deoxy Mb. This indicates that even deoxy H93G(0) has a five-coordinate high-spin iron. In contrast, the iron atom in four-coordinate ferrous heme has $S = 1$

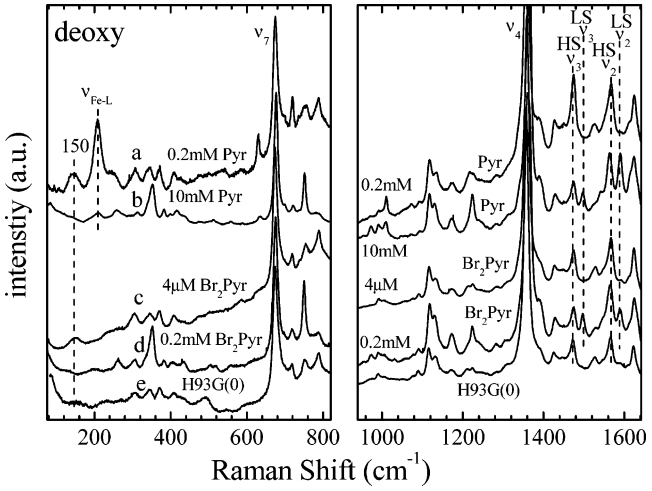


FIGURE 5: Exogenous proximal ligand concentration dependence of the resonance Raman spectra (413.1 nm excitation) of deoxy H93G(Pyr) and H93G($Br_2$Pyr): (a) 0.2 mM Pyr, (b) 10 mM Pyr, (c) 4 $\mu$M $Br_2$Pyr, and (d) saturated $Br_2$Pyr (~0.2 mM). The low-concentration pyridine and dibromopyridine samples are reduced by a factor of 50 from the high-concentration samples. The deoxy H93G(0) spectrum is also shown for comparison (e).

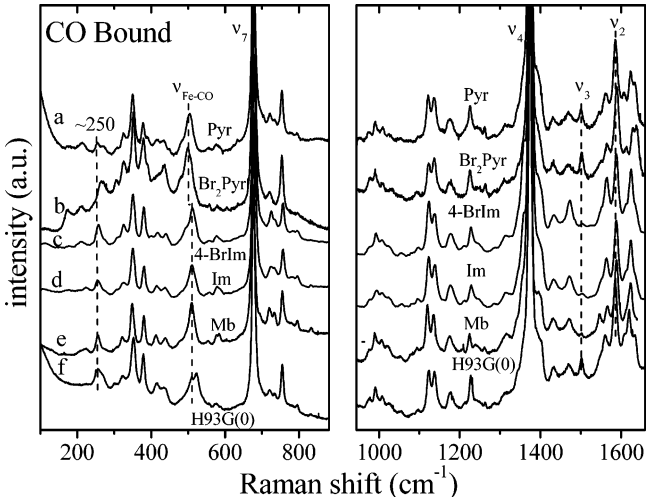


FIGURE 6: cw resonance Raman spectra of CO-bound (a) H93G-(Pyr), (b) H93G($Br_2$Pyr), (c) H93G(4-BrIm), (d) H93G(Im), (e) horse Mb, and (f) H93G(0). The experimental conditions are same as in Figure 3.

and shows distinctive values for the high-frequency marker bands and a Soret absorption near 383 nm (*58*). The axial heme ligand of the five-coordinate heme iron of the H93G-(0) has been proposed to be a water molecule (*31*, *55*).

On the other hand, for H93G(Pyr) and H93G($Br_2$Pyr), $\nu_4$ upshifts 5−9 $cm^{-1}$ relative to horse Mb, while $\nu_3$ and $\nu_2$ show a mixture of high-spin and low-spin species. The absorption spectra of deoxy H93G(Pyr) and H93G($Br_2$Pyr) also have double peaks in the 500−600 nm range, a signature of the six-coordinate low-spin species (*56*). The low-spin feature in deoxy H93G(Pyr) and H93G($Br_2$Pyr) Raman spectra indicates binding of Pyr or $Br_2$Pyr to both proximal and distal sides of the heme iron (vide infra). The Raman spectra in Figure 4 also show some other minor differences for pyridine-based ligands, reflecting an altered iron spin-state equilibrium. This can be seen particularly in the 300−400, 700−800, 950−1000, 1160−1220, and 1600−1640 $cm^{-1}$ regions. When CO is introduced to deoxy H93G(Pyr) or H93G($Br_2$Pyr), it evidently binds to the heme by displacing the distal Pyr or $Br_2$Pyr ligand, if present.

A recent DFT calculation on a five-coordinate Fe(II) porphyrin−pyridine complex reported by Liao et al. (*59*) predicts that (in contrast to histidine ligation) the ground state is low spin. Consequently, we also considered the possibility that H93G(Pyr) and H93G($Br_2$Pyr) are singly ligated (five-coordinate) low spin in the deoxy state. However, when the five-coordinate species is formed, as the pyridine and dibromopyridine concentrations are reduced in the respective samples, the low-spin marker bands disappear in Figure 5 (traces a and c). The Raman spectrum of deoxy H93G(0) is also presented in Figure 5 for comparison. Note that H93G-(Pyr) retains one Pyr ligand when the Pyr concentration is reduced to 0.2 mM. We know this because the Fe−N(Pyr) mode is clearly visible at 208 $cm^{-1}$ in trace a (0.2 mM Pyr), while it is absent in H93G(0) (trace e). We conclude from Figure 5 that the five-coordinate complex of H93G with Pyr is high spin, in disagreement with the DFT prediction (*59*). The ligand coordination state for $Br_2$Pyr is more difficult to assess because there is no obvious Fe−N($Br_2$Pyr) mode. However, the linear superposition of the kinetics shown in Figure 2, along with the low-spin species revealed by the Raman spectra in Figure 5d, strongly suggests one-to-one $Br_2$Pyr ligand binding at the heme.

As shown in Figure 5, the low-concentration dibromopyridine sample (trace c) displays spin markers ($\nu_2$ and $\nu_3$) that are clearly characteristic of five-coordinate high-spin species, but the Fe−N($Br_2$Pyr) mode is absent at both low (trace c) and high (trace d) dibromopyridine concentration. However, the mode at 150 $cm^{-1}$ is stronger for the low-concentration dibromopyridine sample than for the (presumably water-ligated) heme in H93G(0) (trace e). Previous studies (*31*, *60*) suggest that the 150 $cm^{-1}$ mode arises from torsional motions of heterocyclic ligand adducts, which would imply that $Br_2$Pyr is bound as an axial ligand in the five-coordinate species (note the similarity of traces a and c in Figure 5, with the exception of the absence of the Fe−L mode in trace c).

The cw Raman spectra of CO- bound H93G mutants and horse MbCO are shown in Figure 6. The Raman spectra for all CO-ligated H93G mutants and horse MbCO are similar in the 900−1650 $cm^{-1}$ region except that CO−H93G(Pyr) (trace a) and CO−H93G($Br_2$Pyr) (trace b) show a peak at ~1635 $cm^{-1}$. This peak is typical for the $\nu_{10}$ mode of a CO-ligated heme, but it is found to be much weaker in imidazole-based samples and H93G(0). The $\nu_3$ bands near 1475 and 1500 $cm^{-1}$ also show a variation in relative intensity. This effect is consistent with the expected resonance Raman enhancement patterns that arise from the differing excitation wavelengths and the Soret band maxima of pyridine (415 nm) and imidazole (419 nm) ligated heme. All samples in Figure 6 display the ~250 $cm^{-1}$ mode that is associated with the histidine−heme coordination in Mb when CO is ligated (*60*). This is also consistent with $Br_2$Pyr binding to the heme in the H93G($Br_2$Pyr) sample. The similarity of H93G(0) (trace f) with the other spectra in the core size marker band region shown in Figure 6 declares that the CO adduct of H93G(0) is also a six-coordinate low-spin species. Note, however, that two Fe−CO stretching bands are resolved in the Raman spectrum (trace f) in the left panel. Table 4 lists the iron−CO stretching mode ($\nu_{Fe-CO}$) for the samples shown

Table 4: Raman Shift of the Fe−CO Stretching Mode of CO-Bound Ferrous Horse Myoglobin and H93G Mutants with Various Ligands in the Proximal Cavity

| | ligand | | | | | |
|---|---|---|---|---|---|---|
| | Im | 4-BrIm | Pyr | $Br_2$Pyr | 0[a] | His(Mb) |
| $\nu_{Fe-CO}$ ($cm^{-1}$) | 510 | 512 | 505 | 500 | 510, 522 | 510 |

[a] 0 = no added heterocyclic nitrogenous ligand.

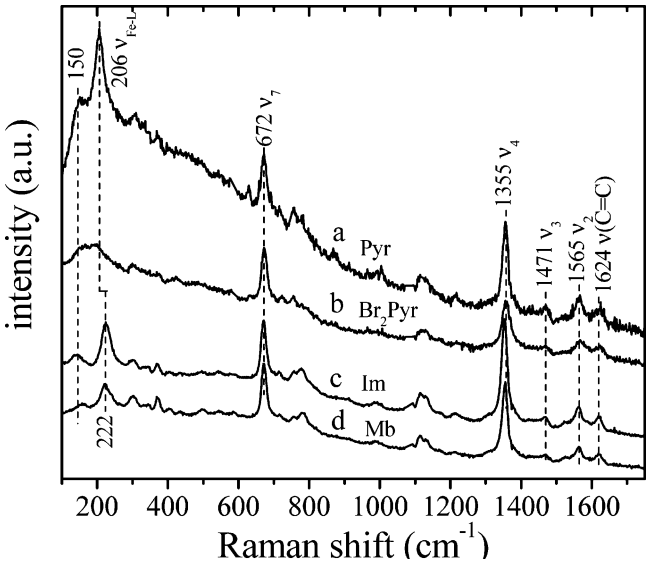


FIGURE 7: Transient Raman spectra of CO-ligated (a) H93G(Pyr), (b) H93G($Br_2$Pyr), (c) H93G(Im), and (d) horse Mb excited by 10 ns, 435.8 nm pulses.

in Figure 6. The Fe−CO stretching mode in CO-bound H93G($Br_2$Pyr), in which the very fast CO rebinding occurs, appears at 500 $cm^{-1}$, a lower frequency than found in the other samples (Table 4).

A situation analogous to the H93G(0) sample may occur in Mb when it is taken to low pH. For example, a previous study (*58*) of low-pH MbCO suggests that a fraction of the sample is ligated by a weak ligand, possibly water, as the proximal ligand. This is consistent with the proposal of Franzen et al. that His-97 can become a proximal heme ligand in the CO complex of H93G(0) and that His-97 switches place with a water molecule during the CO dissociation and rebinding processes (*31*, *55*). The kinetics measurements at 415 nm, shown in Figure 2, reveal a complicated multiphasic process for CO rebinding to H93G(0) (*56*), with a change of sign in $-\Delta A_{415}$ beyond ~100 $\mu$s. The change in sign indicates that CO binding to H93G(0) involves an additional species with a larger absorbance at 415 nm than is present in the CO-bound equilibrium material (which has its Soret maximum at 419 nm). The additional species arises naturally within the "ligand switch" scenario (*31*, *55*) and the Soret band of the transient (e.g., water-bound heme−CO) species is blue shifted from that of the starting material so that the observed negative transmission change at 415 nm can be explained.

Figure 7 shows the 10 ns transient Raman spectra of CO-ligated H93G(Pyr), H93G($Br_2$Pyr), H93G(Im), and horse Mb. For CO-bound H93G(Pyr), H93G(Im), and Mb, the transient spectra indicate that their photoproducts are the corresponding deoxy forms. In contrast, the frequencies of the core size marker bands $\nu_4$, $\nu_3$, and $\nu_2$ indicate that the H93G($Br_2$Pyr) photoproduct is high-spin five-coordinate, rather than the mixture of high- and low-spin forms found in its resting deoxy state (Figure 5d). The very broad peak (in Figure 7b) centered at ~180 $cm^{-1}$ in the CO-dissociated photoproduct of H93G($Br_2$Pyr) is difficult to assign. Its frequency is roughly consistent with the expected Fe−L stretching band due to the mass increase when $Br_2$Pyr replaces Pyr in deoxy H93G (a simple two-body oscillator model predicts an Fe−L mode downshift to 175 $cm^{-1}$). On the other hand, the 180 $cm^{-1}$ feature seems too broad to be a single Fe−N($Br_2$Pyr) stretching mode. It is also noteworthy that the cw Raman measurements of deoxy H93G derivatives reported previously (*57*) show that the Fe−ligand band remains almost unshifted as the mass changes in the series of pyridine-based proximal ligands (L = Pyr, 3-FPyr, 3-MePyr, 3-BrPyr, etc.). In contrast, the Fe−L mode shifts with the expected inverse square root mass dependence for the imidazole-based proximal ligands. The prior assignments involving pyridine-based ligands suggest that if there is an Fe−N($Br_2$Pyr) stretching mode in the photoproduct of CO-bound H93G-($Br_2$Pyr), it should be found near ~207 $cm^{-1}$ (*57*). Overall, these observations appear to rule out the broad ~180 $cm^{-1}$ feature in the CO-dissociated photoproduct of H93G($Br_2$-Pyr) (Figure 7b) as the Fe−N($Br_2$Pyr) stretching mode.

In summary, we emphasize that all of the transient Raman spectra in Figure 7 are very similar except for the Fe−proximal ligand stretch mode. The absence of the Fe−L mode in the $Br_2$Pyr sample reflects a significant proximal perturbation in the photoproduct structure that correlates with a significant increase of the CO geminate rebinding rate in the H93G myoglobin mutant (cf. Figure 1).

## DISCUSSION

Figure 1 and Table 1 show clearly that the proximal ligand significantly influences both geminate and bimolecular rebinding kinetics. Comparison of the CO rebinding parameters in Table 1 reveals that $k_{in}$ in H93G(Im) is about the same as in wild-type Mb; $k_{BA}$ is slightly larger, and $k_{out}$ is almost a factor of 2 smaller. Structurally, the only differences between the wild-type Mb and the H93G(Im) mutant are that H93G(Im) lacks the covalent linkage between the proximal ligand and the protein F-helix. These facts imply that the covalent linkage to the protein backbone has only a small effect on the CO rebinding to Mb at room temperature. The Raman active iron−ligand stretching mode of H93G(Im) is slightly upshifted compared to Mb (Figure 4, Table 3), which has been attributed to the absence of strain from the protein applied to the proximal imidazole in H93G(Im) (*61*). The core-size marker bands for deoxy H93G(Im) and horse Mb are almost the same (Table 3), suggesting that the heme electronic environment is similar for both samples. This is consistent with the observation that the covalent linkage to the protein backbone has a minimal influence on ligand rebinding to Mb. This conclusion is also supported by the early work of Franzen and Boxer (*29*).

In contrast to Mb, there is a large change in ligand binding affinity and cooperativity in the analogous proximally detached mutants of human hemoglobin (*44*, *47*). The well-known Perutz model (*3*) for hemoglobin cooperativity suggests that the protein F-helix strongly controls the distal ligand affinity through the covalent bond between the

proximal ligand and the heme iron atom. This concept has been supported by a variety of experiments (*13*, *44*). In myoglobin, the relatively nonspecific role of the proximal ligand (covalent) linkage to the F-helix suggests that, if the proximal ligand−helix linkage does affect the distal ligand affinity, it must affect the distal ligand dissociation, not the rebinding. In fact, measurements by Kundu et al. (*33*) show that proximal ligand detachment from the helix in Mb decreases the oxygen dissociation rate by a factor of 4 but does not affect the CO dissociation rate.

The crystal structure of wild-type myoglobin shows that the imidazole ring of His-93 nearly eclipses the pyrrole nitrogens of the heme (*17*). On the other hand, the imidazole ring in H93G(Im) is staggered relative to the heme pyrrole nitrogens (*41*). The different orientation of the proximal imidazole ring in wild-type Mb and H93G(Im) apparently has only a small effect on diatomic ligand rebinding. Prior studies of geminate recombination in the H93G mutant system are in very good agreement with this observation (*32*). However, other studies have suggested that the proximal histidine orientation may play a more significant role (*22*, *33*). Nevertheless, the reported bimolecular rebinding and ligand affinity measurements (*22*, *33*), comparing the eclipsed (Mb) and staggered [H93G(Im)] forms, do not actually show effects that can be used to strongly support this suggestion.

We have previously suggested that the geminate rebinding rate depends on a barrier that can be partitioned into a proximal and distal contribution (*7*). The distal contribution presumably involves docking and/or steric barriers that are sensitive to the distal residues, while the proximal contribution has been suggested to depend on the displacement of the high-spin iron from the heme plane (*7*−*10*). The observation that the eclipsed or staggered conformation makes only a minor difference in determining the CO rebinding kinetics suggests that the electronic structure of the iron atom, and the relative strength of its bonds to the porphyrin nitrogens and the proximal ligand, is the major factor that determines the photodissociated heme geometry and the proximal contribution to the geminate rebinding barrier for CO. For example, the geminate rebinding rate, $k_{BA}$, is increased by more than a factor of 2 in H93G(Pyr) compared to H93G(Im). The observed changes in $k_{BA}$ show that small perturbations in the chemical structure of the proximal ligand can definitely affect the CO rebinding.

The Raman spectra of the CO adducts in Figure 6 are all very similar except for the Fe−CO stretching band. It is noteworthy in the above context that the Fe−CO stretching band falls into two classes depending on whether the proximal ligand is pyridine-based or imidazole-based. The fact that the in-plane core-size marker bands are so similar (Table 3) suggests that the different chemical structure of the proximal ligand mainly affects the Fe−axial ligand modes along with the distal ligand rebinding kinetics.

On the other hand, comparing the CO rebinding kinetics among the H93G mutants with the same proximal ligand chemical structure [i.e., H93G(Im) vs H93G(4-BrIm) and H93G(Pyr) vs H93G($Br_2$Pyr)] suggests that the CO geminate rebinding rate $k_{BA}$ increases with the size of the proximal ligand. When $Br_2$Pyr is ligated to H93G Mb, a very large amplitude, fast CO geminate rebinding phase is observed. Therefore, a steric perturbation associated with the size of the proximal ligand can be put forward as one potential reason for changes in the CO rebinding kinetics. For example, it is conceivable that the larger proximal ligand makes it more difficult to achieve a significant iron out of heme plane displacement ($\Delta x$) and that this leads to faster geminate CO rebinding because the proximal contribution to the rebinding barrier ($H_p$) will scale quadratically with this displacement (i.e., $H_p \sim {}^1/_2 k\Delta x^2$) (*7*, *10*).

Most importantly, the rapid geminate rebinding is strongly correlated with the absence of the Fe−N($Br_2$Pyr) stretching band as seen in the CO-dissociated 10 ns transient Raman spectra (Figure 7). Such a correlation may occur if the heme iron stays in plane following CO dissociation and the Franck−Condon coupling needed for resonance Raman activity is reduced (*62*). Another possibility is that the Fe−N($Br_2$Pyr) stretching band is located within the broad ∼180 $cm^{-1}$ feature seen in Figure 7. However, in comparison to other assignments of pyridine-based ligands in H93G (*57*), such a mode frequency would also reflect a significant proximal perturbation. The downshift of the Fe−CO stretching mode to 500 $cm^{-1}$ in CO-bound H93G($Br_2$Pyr) (Table 4) also indicates a change in the heme−proximal ligand geometry or electronic structure. This is because the only difference between the CO-bound H93G($Br_2$Pyr) and H93G(Im) is the different proximal ligand. The changes on the proximal side of the heme appear to be strongly correlated with both the Raman spectra of the axial ligands and the faster CO rebinding kinetics.

Finally, we note that a proximal ligand switching mechanism, similar to an explanation put forward to explain the CO rebinding kinetics of Mb at low pH (*63*, *64*), has also been proposed (*31*, *55*) to describe CO rebinding in H93G(0). This concept is supported by the resonance Raman spectra in Figures 6 and 4. In Figure 6, all CO-ligated species [including the H93G(0) sample] have very similar Raman spectra. This suggests that a similar proximal ligand is present in all species when CO is bound. The binding of CO acidifies the iron in H93G(0) and leads it to coordinate to an internal protein residue (e.g., His-97) (*31*, *55*, *56*). In the absence of CO, the Raman spectrum of deoxy H93G(0) in Figure 4 shows no Fe−His mode, indicating the presence of a different proximal ligand (probably water) in comparison to Mb or H93G(Im). This exchange of proximal ligand in the H93G(0) sample is the likely reason for the complex CO rebinding kinetics displayed in Figure 2. The proximal ligand switching mechanism is also consistent with the negative going $-\Delta A_{415}$ at 100 $\mu$s. This unusual negative going feature will arise if the putative transient (e.g., water bound) species has a strong absorption near 415 nm, where the kinetics are monitored [note that monodisperse CO−protoporphyrin IX in micelles absorbs at 414 nm (*56*)]. Since the CO-bound H93G(0) sample absorbs at 419 nm, the appearance of a transient (water bound) species will lead to stronger absorbance at 415 nm and a negative going $-\Delta A_{415}$ as is observed. Thus, the kinetics displayed in Figure 2 is strongly supportive of the ligand switch mechanism and clearly demonstrates the importance of proximal ligation on the distal ligand rebinding kinetics.

## CONCLUSION

In myoglobin, the linkage connecting the proximal ligand to the F-helix of the protein appears to have only limited

effects on the CO rebinding. On the other hand, the size and chemical structure of the proximal ligand demonstrate a substantial effect on the CO rebinding rate. The rapid rebinding kinetics and Raman spectra associated with the $Br_2$Pyr ligand suggest that steric perturbations of the heme geometry, associated with the size of the proximal ligand, are important; however, proximal ligand-induced electronic perturbations cannot be ruled out as an alternative explanation. The proximal effects on the kinetics described in this work are of the same order as those seen in certain distal pocket double mutants (*27*). This reinforces our original assertion (*7*) that both proximal and distal effects contribute significantly to the CO rebinding barrier at the heme in myoglobin.

Within the set of H93G Mb derivatives presented here, there is a clear correlation observed between the absence of the iron−proximal ligand stretching mode in the photoproduct Raman spectra and very fast CO geminate rebinding. Similar correlations have also been observed (*65*) in studies of microperoxidase (a heme digest of cytochrome *c*). The very fast CO geminate rebinding observed in the H93G($Br_2$-Pyr) Mb mutant is another direct demonstration that proximal perturbations can play a significant role in controlling the geminate phase of ligand rebinding in heme proteins.

## REFERENCES


1. Antonini, E., and Brunori, M. (1971) *Hemoglobin and myoglobin in their reactions with ligands*, North-Holland Publishing Co., Amsterdam and London.
2. Sage, J. T. (2004) Hemoglobins: O2 Uptake and Transport, in *Encyclopedia of Supramolecular Chemistry* (Atwood, J. L., and Steed, J. W., Eds.) pp 636−644, Marcel Dekker, New York.
3. Perutz, M. F. (1970) Stereochemistry of cooperative effects in haemoglobin, *Nature 228*, 726−739.
4. Perutz, M. F. (1979) Regulation of oxygen affinity of hemoglobin: influence of structure of the globin on the heme iron, *Annu. Rev. Biochem. 48*, 327−386.
5. Perutz, M. F., Fermi, G., Luisi, B., Shaanan, B., and Liddington, R. C. (1987) *Acc. Chem. Res. 20*, 309−321.
6. Perutz, M. F. (1990) Mechanisms regulating the reactions of human hemoglobin with oxygen and carbon monoxide, *Annu. Rev. Physiol. 52*, 1−25.
7. Šrajer, V., Reinisch, L., and Champion, P. M. (1988) Protein fluctuations, distributed coupling, and the binding of ligands to heme-proteins, *J. Am. Chem. Soc. 110*, 6656−6670.
8. Šrajer, V., and Champion, P. M. (1991) Investigations of optical-line shapes and kinetic hole burning in myoglobin, *Biochemistry 30*, 7390−7402.
9. Campbell, B. F., Chance, M. R., and Friedman, J. M. (1987) Linkage of functional and structural heterogeneity in proteins—dynamic hole burning in carboxymyoglobin, *Science 238*, 373−376.
10. Ahmed, A. M., Campbell, B. F., Caruso, D., Chance, M. R., Chavez, M. D., Courtney, S. H., Friedman, J. M., Iben, I. E. T., Ondrias, M. R., and Yang, M. (1991) Evidence for proximal control of ligand specificity in hemeproteins—absorption and Raman studies of cryogenically trapped photoproducts of ligand bound myoglobins, *Chem. Phys. 158*, 329−351.
11. Champion, P. M., and Sievers, A. J. (1977) Far infrared magnetic resonance in $FeSiF_6 \cdot 6H_2O$ and $Fe(SPh)^{2-}{}_4$, *J. Chem. Phys. 66*, 1819−1825.
12. Champion, P. M. and Sievers, A. J. (1980) Far infrared magnetic resonance of deoxyhemoglobin and deoxymyoglobin, *J. Chem. Phys. 72*, 1569−1582.
13. Perutz, M. F., Wilkinson, A. J., Paoli, M., and Dodson, G. G. (1998) The stereochemical mechanism of the cooperative effects in hemoglobin revisited, *Annu. Rev. Biophys. Biomol. Struct. 27*, 1−34.
14. Olson, J. S., Mathews, A. J., Rohlfs, R. J., Springer, B. A., Egeberg, K. D., Sligar, S. G., Tame, J., Renaud, J. P., and Nagai, K. (1988) The role of the distal histidine in myoglobin and haemoglobin, *Nature 336*, 265−266.
15. Rohlfs, R. J., Mathews, A. J., Carver, T. E., Olson, J. S., Springer, B. A., Egeberg, K. D., and Sligar, S. G. (1990) The effects of amino acid substitution at position E7 (residue 64) on the kinetics of ligand binding to sperm whale myoglobin, *J. Biol. Chem. 265*, 3168−3176.
16. Carver, T. E., Rohlfs, R. J., Olson, J. S., Gibson, Q. H., Blackmore, R. S., Springer, B. A., and Sligar, S. G. (1990) Analysis of the kinetic barriers for ligand-binding to sperm whale myoglobin using site-directed mutagenesis and laser photolysis techniques, *J. Biol. Chem. 265*, 20007−20020.
17. Quillin, M. L., Arduini, R. M., Olson, J. S., and Phillips, G. N., Jr. (1993) High-resolution crystal structures of distal histidine mutants of sperm whale myoglobin, *J. Mol. Biol. 234*, 140−155.
18. Springer, B., Sligar, S. G., Olson, J. S., and Phillips, G. N., Jr. (1994) mechanisms of ligand recognition in myoglobin, *Chem. Rev. 94*, 699−714.
19. Olson, J. S., and Phillips, G. N., Jr. (1996) Kinetic pathways and barriers for ligand binding to myoglobin, *J. Biol. Chem. 271*, 17593−17596.
20. Thorsteinsson, M. V., Bevan, D. R., Potts, M., Dou, Y., Eich, R. F., Hargrove, M. S., Gibson, Q. H., and Olson, J. S. (1999) A cyanobacterial hemoglobin with unusual ligand binding kinetics and stability properties, *Biochemistry 38*, 2117−2126.
21. Dou, Y., Maillett, D. H., Eich, R. F., and Olson, J. S. (2002) Myoglobin as a model system for designing heme protein based blood substitutes, *Biophys. Chem. 98*, 127−148.
22. Draghi, F., Miele, A. E., Travaglini-Allocatelli, C., Vallone, B., Brunori, M., Gibson, Q. H., and Olson, J. S. (2002) Controlling ligand binding in myoglobin by mutagenesis, *J. Biol. Chem. 277*, 7509−7519.
23. Nienhaus, K., Deng, P., Olson, J. S., Warren, J. J., and Nienhaus, G. U. (2003) Structural dynamics of myoglobin: ligand migration and binding in valine 68 mutants, *J. Biol. Chem. 278*, 42532−42544.
24. Schotte, F., Lim, M., Jackson, T. A., Smirnov, A. V., Soman, J., Olson, J. S., Phillips, G. N., Jr., Wulff, M., and Anfinrud, P. A. (2003) Watching a protein as it functions with 150-ps time-resolved X-ray crystallography, *Science 300*, 1944−1947.
25. Olson, J. S., Foley, E. W., Maillett, D. H., and Paster, E. V. (2003) Measurement of rate constants for reactions of O2, CO, and NO with hemoglobin, *Methods Mol. Med. 82*, 65−91.
26. Unno, M., Matsui, T., Chu, G. C., Couture, M., Yoshida, T., Rousseau, D. L., Olson, J. S., and Ikeda-Saito, M. (2004) Crystal structure of the dioxygen-bound heme oxygenase from *Corynebacterium diphtheriae*: Implications for heme oxygenase function, *J. Biol. Chem.* (in press).
27. Sugimoto, T., Unno, M., Shiro, Y., Dou, Y., and Ikeda-Saito, M. (1998) Myoglobin mutants giving the largest geminate yield in CO rebinding in the nanosecond time domain, *Biophys. J. 75*, 2188−2194.
28. Decatur, S. M., DePillis, G. D., and Boxer, S. G. (1996) Modulation of protein function by exogenous ligands in protein cavities: CO binding to a myoglobin cavity mutant containing unnatural proximal ligands, *Biochemistry 35*, 3925−3932.
29. Franzen, S., and Boxer, S. G. (1997) On the origin of heme absorption band shifts and associated protein structural relaxation in myoglobin following flash photolysis, *J. Biol. Chem. 272*, 9655−9660.
30. Cao, W., Sjodin, T., Sage, J. T., Ye, X., Demidov, A. A., Wang, W., Champion, P. M., and Barrick, D. (2001) Proximal and distal influences on ligand binding to heme proteins, *Biophys. J. 80*, 283a.
31. Franzen, S., Bailey, J., Dyer, R. B., Woodruff, W. H., Hu, R. B., Thomas, M. R., and Boxer, S. G. (2001) A photolysis-triggered heme ligand switch in H93G myoglobin, *Biochemistry 40*, 5299−5305.
32. Franzen, S. (2002) Carbonmonoxy rebinding kinetics in H93G myoglobin: Separation of proximal and distal side effects, *J. Phys. Chem. B 106*, 4533−4542.
33. Kundu, S., Snyder, B., Das, K., Chowdhury, P., Park, J., Petrich, J. W., and Hargrove, M. S. (2002) The leghemoglobin proximal heme pocket directs oxygen dissociation and stabilizes bound heme, *Proteins 46*, 268−277.
34. Sage, J. T., and Champion, P. M. (1996) Small Substrate Recognition in Heme Proteins, in *Comprehensive Supramolecular Chemistry* (Suslick, K. S., Ed.) pp 171−218, Pergamon, Oxford, U.K.

35. Harvey, J. N. (2000) DFT Computation of the intrinsic barrier to CO geminate recombination with heme compounds, *J. Am. Chem. Soc. 122*, 12401−12402.
36. McMahon, B. H., Stojkovic, B. P., Hay, P. J., Martin, R. L., and Garcia, A. E. (2000) Microscopic model of carbon monoxide binding to myoglobin, *J. Chem. Phys. 113*, 6831−6850.
37. Kumazaki, S., Nakajima, H., Sakaguchi, T., Nakagawa, E., Shinohara, H., Yoshihara, K., and Aono, S. (2000) Dissociation and recombination between ligands and heme in a CO-sensing transcriptional activator CooA. A flash photolysis study, *J. Biol. Chem. 275*, 38378−38383.
38. Duprat, A. F., Traylor, T. G., Wu, G. Z., Coletta, M., Sharma, V. S., Walda, K. N., and Magde, D. (1995) Myoglobin NO at low pH−free 4-coordinated heme in the protein pocket, *Biochemistry 34*, 2634−2644.
39. Miers, J. B., Postlewaite, J. C., Cowen, B. R., Roemig, G. R., Lee, I. Y. S., and Dlott, D. D. (1991) Preexponential-limited solid-state chemistry−ultrafast rebinding of a heme ligand complex in a glass or protein matrix, *J. Chem. Phys. 94*, 1825−1836.
40. Austin, R. H., Beeson, K. W., Eisenstein, L., Frauenfelder, H., and Gunsalus, I. C. (1975) Dynamics of ligand binding to myoglobin, *Biochemistry 14*, 5355−5373.
41. Barrick, D. (1994) Replacement of the proximal ligand of sperm whale myoglobin with free imidazole in the mutant His-93 → Gly, *Biochemistry 33*, 6546−6554.
42. DePillis, G. D., Decatur, S. M., Barrick, D., and Boxer, S. G. (1994) Functional cavities in proteins: A general method for proximal ligand substitution in myoglobin, *J. Am. Chem. Soc. 116*, 6981−6982.
43. Barrick, D. (1995) Depletion and replacement of protein metal ligands, *Curr. Opin. Biotechnol. 6*, 411−418.
44. Barrick, D., Ho, N. T., Simplaceanu, V., Dahlquist, F. W., and Ho, C. (1997) A test of the role of the proximal histidines in the Perutz model for cooperativity in haemoglobin, *Nat. Struct. Biol. 4*, 78−83.
45. Barrick, D., and Dahlquist, F. W. (2000) Trans-substitution of the proximal hydrogen bond in moglobin: I. Structural consequences of hydrogen bond deletion, *Proteins: Struct., Funct., Genet. 39*, 278−290.
46. Barrick, D. (2000) Trans-substitution of the proximal hydrogen bond in moglobin: II. Energetics, functional consequences, and implications for hemoglobin allostery, *Proteins: Struct., Funct., Genet. 39*, 291−308.
47. Barrick, D., Ho, N. T., Simplaceanu, V., and Ho, C. (2001) Distal ligand reactivity and quaternary structure studies of proximally detached hemoglobins, *Biochemistry 40*, 3780−3795.
48. Cao, W., Christian, J. F., Champion, P. M., Rosca, F., and Sage, J. T. (2001) Water penetration and binding to ferric myoglobin, *Biochemistry 40*, 5728−5737.
49. Christian, J. F., Unno, M., Sage, J. T., Champion, P. M., Chien, E., and Sligar, S. G. (1997) Spectroscopic effects of polarity and hydration in the distal heme pocket of deoxymyoglobin, *Biochemistry 36*, 11198−11204.
50. Peterson, E. S., and Friedman, J. M. (1998) A possible allosteric communication pathway identified through a resonance Raman study of four beta 37 mutants of human hemoglobin A, *Biochemistry 37*, 4346−4357.
51. Henry, E. R., Sommer, J. H., Hofrichter, J., and Eaton, W. A. (1983) Geminate recombination of carbon-monoxide to myoglobin, *J. Mol. Biol. 166*, 443−451.
52. Seidell, A. (1940) *Solubilities of inorganic and metal organic compounds; a compilation of quantitative solubility data from the periodical literature*, D. Van Nostrand Co., New York.
53. Kumar, A. T. N., Zhu, L., Christian, J. F., Demidov, A. A., and Champion, P. M. (2001) On the rate distribution analysis of kinetics data using the maximum entropy method: application to myoglobin relaxation on the nanosecond and femtosecond time scales, *J. Phys. Chem. B 105*, 7847−7856.
54. Springer, B. A., Sligar, S. G., Olson, J. S., and Phillips, G. N., Jr. (1994) Mechanisms of ligand recognition in myoglobin, *Chem. Rev. 94*, 699−714.
55. Franzen, S., Peterson, E. S., Brown, D., Friedman, J. M., Thomas, M. R., and Boxer, S. G. (2002) Proximal ligand motions in H93G myoglobin, *Eur. J. Biochem. 269*, 4879−4886.
56. Cao, W. (2003) Laser flash photolysis and resonance raman investigations of ligand rebinding to heme proteins, Ph.D. Dissertation, Northeastern University, Boston, MA.
57. Franzen, S., Boxer, S. G., Dyer, R. B., and Woodruff, W. H. (2000) Resonance raman studies of heme axial ligation in H93G myoglobin, *J. Phys. Chem. B 104*, 10359−10367.
58. Sage, J. T., Morikis, D., and Champion, P. M. (1991) Spectroscopic studies of myoglobin at low pH−heme structure and ligation, *Biochemistry 30*, 1227−1237.
59. Liao, M.-S., and Scheiner, S. (2002) Electronic structure and bonding in unligated and ligated FeII porphyrins, *J. Chem. Phys. 116*, 3635−3645.
60. Wells, A. V., Sage, J. T., Morikis, D., Champion, P. M., Chiu, M. L., and Sligar, S. G. (1991) The iron histidine mode of myoglobin revisited−resonance Raman studies of isotopically labeled *Escherichia coli* expressed myoglobin, *J. Am. Chem. Soc. 113*, 9655−9660.
61. Uchida, T., Ishikawa, H., Ishimori, K., Morishima, I., Nakajima, H., Aono, S., Mizutani, Y., and Kitagawa, T. (2000) Identification of histidine 77 as the axial heme ligand of carbonmonoxy CooA by picosecond time-resolved resonance Raman spectroscopy, *Biochemistry 39*, 12747−12752.
62. Bangcharoenpaurpong, O., Schomacker, K. T., and Champion, P. M. (1984) A resonance Raman investigation of myoglobin and hemoglobin, *J. Am. Chem. Soc. 106*, 5688−5698.
63. Sage, J. T., Li, P. S., and Champion, P. M. (1991) Spectroscopic studies of myoglobin at low pH−heme ligation kinetics, *Biochemistry 30*, 1237−1247.
64. Sage, J. T., Morikis, D., Li, P. S., and Champion, P. M. (1992) Low pH myoglobin photoproducts, *Biophys. J. 61*, 1041−1044.
65. Cao, W., Ye, X., Georgiev, G. Y., Berezhna, S., Sjodin, T., Demidov, A. A., Wang, W., Sage, J. T., and Champion, P. M. (2004) Proximal and distal influences on ligand binding kinetics in microperoxidase and heme model compounds, *Biochemistry 43*, 7017−7027.

BI049077G